International Journal of Nanomedicine

Dovepress
Taylor & Francis Group

Open Access Full Text Article

ORIGINAL RESEARCH

Biomimetic Nanoplatform Based on Macrophage Membrane-Coated Fe3O4 Nanoparticles for Synergistic Ferroptosis and Sonodynamic Therapy of Lung Cancer

Hongming Zhang[1,*], Yu Zhuang[2,*], Jianxiang Song[3], Feng Shao[2], Woda Shi[3]

[1]Department of Pneumology, Affiliated Hospital 6 of Nantong University, The Yancheng School of Clinical Medicine of Nanjing Medical University, Yancheng Third People's Hospital, Yancheng, Jiangsu, 224000, People's Republic of China; [2]Department of Thoracic Surgery, Nanjing Chest Hospital, Affiliated Nanjing Brain Hospital, Nanjing Medical University, Nanjing, Jiangsu, 210029, People's Republic of China; [3]Department of Cardiothoracic Surgery, Affiliated Hospital 6 of Nantong University, The Yancheng School of Clinical Medicine of Nanjing Medical University, Yancheng Third People's Hospital, Yancheng, Jiangsu, 224000, People's Republic of China

*These authors contributed equally to this work

Correspondence: Feng Shao, Nanjing Chest Hospital, Affiliated Nanjing Brain Hospital, Nanjing Medical University, No. 215 Guangzhou Road, Nanjing, 210029, People's Republic of China, Email doctorshao1982@sina.com; Woda Shi, Department of Cardiothoracic Surgery, Affiliated Hospital 6 of Nantong University, The Yancheng School of Clinical Medicine of Nanjing Medical University, Yancheng Third People's Hospital, No. 75 Juchang Road, Yancheng, Jiangsu, 224000, People's Republic of China, Email xuelangziyao@163.com

Introduction: Triiron tetraoxide nanoparticles (Fe3O4 NPs) effectively induce ferroptosis. However, they are readily identified as foreign by the immune system and undergo rapid clearance from the body via the reticuloendothelial system. Macrophages are a type of phagocytic immune cell. They identify and engulf cancer cells and any foreign entities that lack the specific surface biomarkers of healthy somatic cells. Studies have proposed that camouflaging NPs with macrophage membranes enables effective cancer targeting via cell-cell adhesion mechanisms.

Methods: Therefore, we harvested vesicles derived from macrophage membranes and coated them onto the surface of Fe3O4 nanoparticles. This formed a core-shell, biomimetic nanodrug delivery system: Fe3O4@MPs. Subsequently, we loaded hematoporphyrin monomethyl ether (HMME) onto this platform (Fe3O4-HMME@MPs). The nanoparticles were comprehensively characterized. Their in vitro performance, including cellular uptake, reactive oxygen species generation, ferrous ions (Fe^{2+}) release, and cytotoxicity, was evaluated using A549 lung cancer cells. For in vivo studies, a subcutaneous xenograft model was established in nude mice using A549 cells. The tumor-targeting ability was assessed via fluorescence imaging, and the therapeutic efficacy was systematically evaluated by monitoring tumor volume/weight, histopathological analysis, and immunohistochemical staining (Perls-DAB, TUNEL, Ki67, GPX4).

Results: Characterization of the NPs, along with in vivo and in vitro experiments, confirmed that Fe3O4-HMME@MPs possess excellent biocompatibility, immune evasion capabilities, and effective targeting of lung tumors. Fe3O4-HMME@MPs treat solid lung tumors through a synergistic of ferroptosis and Sonodynamic therapy.

Conclusion: Our platform provides us with a novel biomimetic strategy, offering a promising approach for clinical translation in lung cancer therapy.

Keywords: triiron tetraoxide nanoparticles, sonodynamic therapy, lung cancer, ferroptosis, macrophage membrane

Introduction

Lung cancer is the second most commonly diagnosed cancer globally and the leading cause of cancer-related mortality.[1,2] Epidemiological data indicate that over 2.2 million new cases of lung cancer occur worldwide, a figure projected to continue rising.[3] China alone accounts for more than one-third of global new cases and nearly 40% of deaths,

https://doi.org/10.2147/IJN.S573349
Received: 10 October 2025
Accepted: 30 December 2025
Published: 13 January 2026

highlighting the significant regional health challenge posed by lung cancer.[4] Lung cancer patients generally exhibit poor clinical prognosis, with a five-year survival rate below 25%. This is primarily attributed to its rapid disease progression, strong propensity for distant metastasis, and often late-stage diagnosis, factors that contribute to suboptimal treatment outcomes.[5] For early-stage patients, surgical resection remains the primary curative treatment option.[6] In recent years, significant advancements have been made in the treatment of advanced lung cancer, with therapies including immune checkpoint inhibitors, tyrosine kinase inhibitors, and platinum-based chemotherapy yielding notable clinical benefits.[7] However, challenges persist in overall prognosis due to severe side effects of chemotherapy, acquired resistance to targeted therapy, and limited response rates to immunotherapy in some patients.[3,8] Therefore, there is an urgent and critical need to develop novel therapeutic strategies that are both highly effective and low-toxicity, particularly as alternative or adjuvant therapies.

In recent years, novel therapies based on metallic nanomaterials have emerged as a highly promising strategy for the treatment of various cancers. Among these materials, triiron tetraoxide nanoparticles (Fe3O4 NPs) have garnered significant attention owing to their excellent biocompatibility and established clinical safety.[9] Their translation to clinical practice is underscored by approvals from regulatory bodies, including the US FDA and the European Union, for applications such as magnetic resonance imaging contrast agents and the treatment of glioblastoma.[10,11] The therapeutic mechanism of Fe3O4 NPs is primarily rooted in their intrinsic peroxidase-like activity. Within the acidic tumor microenvironment, they can catalyze endogenous hydrogen peroxide (H_2O_2) to generate highly cytotoxic hydroxyl radicals (•OH) via a Fenton-like reaction.[12,13] Furthermore, following cellular internalization, Fe3O4 NPs undergo degradation within lysosomes, releasing a substantial amount of iron ions. This process not only amplifies the aforementioned catalytic reaction but also disrupts intracellular iron homeostasis, thereby inducing ferroptosis.[14] In addition to their chemical catalytic activity, the superparamagnetic properties of Fe3O4 NPs endow them with a unique physical targeting capability.[15] This enables their accumulation at the tumor site to be significantly enhanced under the guidance of an external magnetic field. However, the biomedical application of bare Fe3O4 NPs is met with critical challenges. They are susceptible to aggregation under physiological conditions, leading to poor colloidal stability, and are subject to rapid clearance by the reticuloendothelial system, which severely limits their therapeutic efficacy.[16]

Sonodynamic therapy (SDT) is an emerging non-invasive therapeutic strategy.[17] It skillfully combines the physical properties of ultrasound (US) with the chemical action of sonosensitizers.[18] Within the tumor microenvironment, SDT precisely induces cytotoxic effects, opening a new avenue for the treatment of cancers such as breast, primary liver, and pancreatic cancer.[19–21] Compared to conventional radiotherapy and chemotherapy, SDT offers numerous distinct advantages. This is primarily due to the excellent tissue-penetrating capability of US. Furthermore, as a non-invasive therapeutic modality, SDT reduces patient discomfort and risks. Hematoporphyrin monomethyl ether (HMME) is a semi-synthetic porphyrin derivative. It is widely employed in SDT.[22] HMME produces reactive oxygen species (ROS) through the efficient absorption of US energy. This, in turn, induces the selective apoptosis of cancer cells. However, the therapeutic efficacy of SDT is severely hampered by the prevalent hypoxia within the tumor. This condition significantly suppresses the generation of ROS, thus constituting a major therapeutic bottleneck.

Macrophages are a type of phagocytic immune cell. They identify and engulf cancer cells and any foreign entities that lack the specific surface biomarkers of healthy somatic cells.[23] We utilized macrophage membranes to coat Fe3O4 nanoparticles loaded with the sonosensitizer HMME, successfully fabricating the biomimetic nanosystem Fe3O4-HMME@MPs. This study confirmed that the nanoparticle possesses excellent biocompatibility, immune evasion capabilities, and precise targeting of lung tumors. It is capable of effectively treating solid lung tumors through synergistic ferroptosis and SDT.

Materials and Methods

Solvothermal Synthesis of Fe3O4 NPs

0.648 g of anhydrous ferric chloride (FeCl3) and 0.48 g of trisodium citrate dihydrate (Na3Cit) were dissolved in diethylene glycol (40 mL). The mixture was stirred vigorously at 80°C. After the solution became clear, 1.0 g of anhydrous sodium acetate (NaAc) was added. Stirring was continued until it was dissolved. Subsequently, the mixture was transferred into a Teflon-lined stainless-steel autoclave and maintained at 200 °C for 10 h to obtain 4 nm Fe3O4 NPs.

The as-prepared Fe3O4 NPs were washed repeatedly with anhydrous ethanol and distilled water. Finally, they were stored in deionized water for further use.

Cell Culture

The human NSCLC cell line (A549) was purchased from the China Cell Center (Shanghai, China). The cells were resuscitated and treated after receipt according to the manufacturer's instructions. The A549 cell line was cultured in Dulbecco's Modified Eagle Medium (DMEM; Gibco) supplemented with 10% FBS and 100 U/mL penicillin–streptomycin in a 5% CO_2 incubator.

Extraction of Macrophage Membranes

Macrophage cells were placed in ice-cold Tris-magnesium buffer (TM buffer, pH 7.4, 0.01 M Tris and 0.001 M $MgCl_2$). The cells were disrupted by extrusion through a mini-extruder 20 times without a polycarbonate membrane. The cell homogenate was mixed with 1 M sucrose to a final concentration of 0.25 M sucrose. The mixture was centrifuged at 2000 ×g for 10 min at 4 °C. The supernatant was collected and further centrifuged at 3,000 ×g for 30 min at 4 °C to collect the cell membranes. The cell membranes were washed with ice-cold TM buffer containing 0.25 M sucrose and collected by centrifugation at 3,000 ×g for 30 min at 4 °C. The protein content in the purified macrophage membranes was determined by the BCA protein assay.

Preparation of Fe3O4@MPs

A PBS solution containing 50 μg of Fe3O4 NPs and 150 μg of cell membranes was mixed and agitated overnight (membrane-to-nanoparticle mass ratio = 3:1). The mixture was then extruded 11 times through a 200 nm membrane using an extruder. Finally, the resulting Fe3O4@MPs were stored in PBS at 4 °C for further use.

Characterization of Fe3O4-HMME@MPs

The crystalline structure of the bare Fe3O4 NPs was analyzed by X-ray diffraction (XRD) using Malvern Panalytical Aeris X-ray diffractometer (Netherlands) operating at 40 kV and 35 mA. Elemental composition and chemical states were analyzed by X-ray photoelectron spectroscopy (XPS) using Thermo Scientific K-Alpha X X-ray Photoelectron Spectrometer. The morphologies of Fe3O4 NPs and Fe3O4-HMME@MPs were characterized by transmission electron microscopy (TEM, Tecnai-12, Philips, Eindhoven, Netherlands) at an accelerating voltage of 120 kV. The hydrodynamic size distribution of Fe3O4-HMME@MPs in aqueous suspension was determined by dynamic light scattering (DLS, Zetasizer Nano ZS, Malvern Instruments, Malvern, UK) at 25°C. Fourier-transform infrared (FTIR) spectra of HMME, Fe3O4 NPs, MPs, and Fe3O4-HMME@MPs were recorded using an FTIR spectrometer (Nicolet iS50, Thermo Fisher Scientific, Waltham, MA, USA) in the range of 400–4000 cm^{-1} to confirm HMME loading and membrane coating. Sodium dodecyl sulfate-polyacrylamide gel electrophoresis (SDS-PAGE) was performed to analyze the protein profiles of the raw macrophage cell membrane, Fe3O4 NPs, and the Fe3O4@MPs. Gels were stained with Coomassie Brilliant Blue to visualize the protein bands.

HMME Loading and in vitro Drug Release Study

1 mL of Fe3O4 NPs (2 mg/mL) was co-incubated with 500 μg of HMME (4 mg/mL in DMSO) overnight with agitation. After centrifugal ultrafiltration, the drug loading content of 4.8% and encapsulation efficiency of 24.2% were determined by measuring the UV-vis absorbance of the filtrate (121.14 μg loaded per 500 μg of initial HMME and 2 mg of NPs).

For the release study, the Fe3O4-HMME solution was dispersed in PBS at pH 5.0 and 7.4 and shaken, with or without US treatment. At different time points (0.5, 1, 2, 4, 6, 12, 24 h), the solution was centrifuged. The filtrate was collected, and the extent of drug release was evaluated by measuring the UV-vis absorbance.

In vitro Radical Generation

Quantification of Fe^{2+} Release: Fe3O4 NPs (1 mL, 2 mg/mL) were incubated in 1 mL of PBS (pH 5.0 or 7.4) for 12 h. The filtrate was collected via ultrafiltration and titrated with a 0.1 M potassium permanganate solution. The titration

was stopped when the solution turned from colorless to a faint purple or pink that persisted for 30s. The amount of released Fe^{2+} was calculated based on the reaction equation ($Mn^{2+} + 5Fe^{2+} + 8H^{+} \rightarrow Mn^{2+} + 5Fe^{3+} + 4H_2O$).

OH Detection

Fe3O4-HMME was dispersed in an acetate buffer (pH 5.0) to achieve an HMME concentration of 5 μg/mL. After adding 100 μL of H_2O_2 solution (1 M), the mixture was allowed to react for 2 h. Then, 200 μL of 3-CCA solution (1 mM) was added, followed by US irradiation (1 MHz, 2 W/cm^2) for 5 min. The reaction was continued for another 30 min. Spectra were measured using a fluorescence spectrophotometer (for 3-CCA: ex/em = 350/450 nm).

ROS Detection

Fe3O4-HMME was prepared in a series of concentrations (2, 4, 6, 8, 10 μg/mL, based on HMME concentration). An equal volume of DPCI solution was added and mixed. After US irradiation (1 MHz, 2 W/cm^2) for 5 min, 4 mL of chloroform was added for extraction over 48 h. The absorbance of the chloroform layer was measured at 563 nm using a UV-vis spectrophotometer.

MTT Assay for Cytotoxicity

Dark Toxicity: A549 cells were seeded into 96-well plates. 100 μL of medium containing different concentrations of Fe3O4 NPs (0, 50, 100, 200, 400, 800 μg/mL), free HMME, and Fe3O4-HMME@MPs (0, 2.5, 5, 10, 20, 40 μg/mL, based on HMME concentration) were added to each well. After a 24 h incubation, the absorbance was measured.

Sonotoxicity: Cells were treated with free HMME, Fe3O4-HMME, and Fe3O4-HMME@MPs (all at an HMME concentration of 20 μg/mL) with or without US irradiation (1 MHz, 2 W/cm^2, 5 min). After an initial 4 h incubation, the cells were further incubated for 20 h before measuring the absorbance.

Cellular Uptake

Cellular uptake was assessed in A549 cells. Cells were incubated with free HMME for 4 h, and with Fe3O4-HMME and Fe3O4-HMME@MPs for 1 h and 4 h, respectively. Images were captured using a confocal laser scanning microscope.

Intracellular •OH and ROS Generation Assay

Cells were incubated with HMME, Fe3O4-HMME, and Fe3O4-HMME@MPs for 4 h, followed by treatment with or without US. The cells were then stained with DCFH-DA and 3-CCA. Images were captured by CLSM and quantified using ImageJ.

In vivo Biodistribution

Nude mice (BALB/C-nu/nu) were divided into two groups (Fe3O4-HMME and Fe3O4-HMME@MPs, n=5 per group). At five time points (2, 6, 12, 24, 48 h), nude mice were sacrificed. Organs were imaged using an in vivo imaging system. In vivo animal experimentation was performed at the Jiangsu University Laboratory Animal Research Center. This work was under the supervision and received the approval of the Jiangsu University Committee on Laboratory Animal Management and Use (IACUC Number: KY-20230127).

In vivo Antitumor Therapy

Nude mice (BALB/C-nu/nu) were randomized into 8 groups (n=5 per group). Logarithmically growing A549 cells were washed with PBS (pH 7.4). Subsequently, cells were subcutaneously injected into the right forelimb axillary region of nude mice at a density of 1×10^7 cells per mouse. After tumor formation, drugs were administered via tail vein injection every other day. US treatment was applied 4 h and 12 h post-injection. Tumor-bearing nude mice were randomly assigned to six groups, receiving either (a) PBS; (b) Fe3O4-NP (20 mg/kg); (c) HMME (5 mg/kg); (d) HMME + US; (e) Fe3O4@MPs (20 mg/kg); (f) Fe_3O_4@MPs + US; (g) Fe3O4-HMME@MPs (at HMME dosage of 5 mg/kg); or (h) Fe3O4-HMME@MPs + US. For final analysis and subsequent illustrations, three representative tumors per group were selected (n=3). Tumor volume and body weight were recorded during the treatment period. Tumor sizes were measured

every 2 days using calipers and calculated using the formula: Volume = (tumor length) × (tumor width)^2/2. At the end of the experiment, all nude mice were humanely euthanized by cervical dislocation, in accordance with international animal welfare guidelines (eg, AVMA Guidelines). Following euthanasia, mice were immediately dissected, and tumors were excised, weighed, and photographed. Tissues and tumors were subjected to H&E staining. Immunohistochemical staining for Perls-DAB, TUNEL, Ki67, and GPX4 was performed on tumors from each group.

Statistical Analysis

Data were analyzed using SPSS 16.0 software. The data were expressed as the mean ± standard deviation from at least three independent replicate experiments. One-way analysis of variance was used to calculate statistical differences between groups. A p-value of <0.05 was considered to indicate a statistically significant difference.

Results

Characterization of Fe3O4 NPs and Fe3O4@MPs

To confirm the successful fabrication of the biomimetic NPs, their morphology was first examined by transmission electron microscopy. As shown in Figure 1a, the as-prepared bare Fe3O4 NPs were uniform spheres with an average diameter of approximately 10 nm. Following encapsulation with MPs, the resulting Fe3O4@MPs exhibited a distinct core-shell structure, where a core of aggregated Fe3O4 NPs was enveloped by an intact cell membrane shell (Figure 1b). This structural transformation was further corroborated by dynamic light scattering and zeta potential measurements. DLS analysis revealed a significant increase in the hydrodynamic diameter from ~15 nm for the bare Fe3O4 NPs to ~160 nm for Fe3O4@MPs (Figure 1c). Crucially, the successful membrane coating was evidenced by a reversal in surface charge: the initially positive zeta potential of the bare Fe3O4 NPs shifted to a negative value for Fe3O4@MPs, closely resembling that of the source cell membranes (Figure 1d). Furthermore, the physicochemical properties of the Fe3O4 NPs were characterized. The X-ray diffraction pattern confirmed their well-defined crystalline structure (Figure 1e), while X-ray photoelectron spectroscopy verified the elemental composition of Fe and O (Figure 1f). Finally, the successful loading of HMME was confirmed through spectroscopic analysis. Both the UV-vis absorption and Fourier-transform infrared spectra of the final product, Fe3O4-HMME, displayed characteristic absorption peaks corresponding to both the Fe3O4 NP core and the HMME drug (Figure 1g and h). Taken together, these results confirm the successful fabrication of Fe3O4@MPs with an intact core-shell structure and effective drug encapsulation.

In vitro Functional Characterization of Fe3O4@MPs

To systematically evaluate the functionality of the as-fabricated biomimetic NPs, a series of in vitro experiments were performed. First, the drug release behavior was investigated. A standard curve was established for quantifying HMME release (Figure 2a). As shown in Figure 2b, the cumulative release of HMME was significantly faster under acidic conditions (pH 5.0) compared to physiological pH (7.4), and this process was further accelerated by US treatment. Next, SDS-PAGE analysis confirmed the successful preservation of membrane proteins following the coating process. The protein profile of Fe3O4@MPs (Lane 3) was nearly identical to that of the source cell membranes (Lane 2), indicating a successful transfer of the membrane's functional components (Figure 2c). We then evaluated the pH-responsive release of Fe^{2+} from the Fe3O4 core, which is crucial for subsequent Fenton-like reactions. Consistent with the acidic tumor microenvironment, a greater amount of Fe^{2+} was released at pH 5.0 than at neutral pH (Figure 2d). The generation of hydroxyl radicals (•OH), a key cytotoxic species in sonodynamic therapy, was monitored using a coumarin-3-carboxylic acid (CCA) fluorescent probe. Following US irradiation, the Fe3O4-HMME group produced a significantly higher amount of •OH compared to the free HMME group, as indicated by the enhanced fluorescence intensity (Figure 2e). Finally, the overall generation of ROS was assessed. We observed a concentration-dependent increase in ROS levels in cells treated with Fe3O4-HMME. Notably, at concentrations of 6 μg/mL and above, the combination of Fe3O4-HMME with US irradiation resulted in a significantly higher ROS level than that produced by Fe3O4-HMME alone (Figure 2f).

https://doi.org/10.2147/IJN.S573349

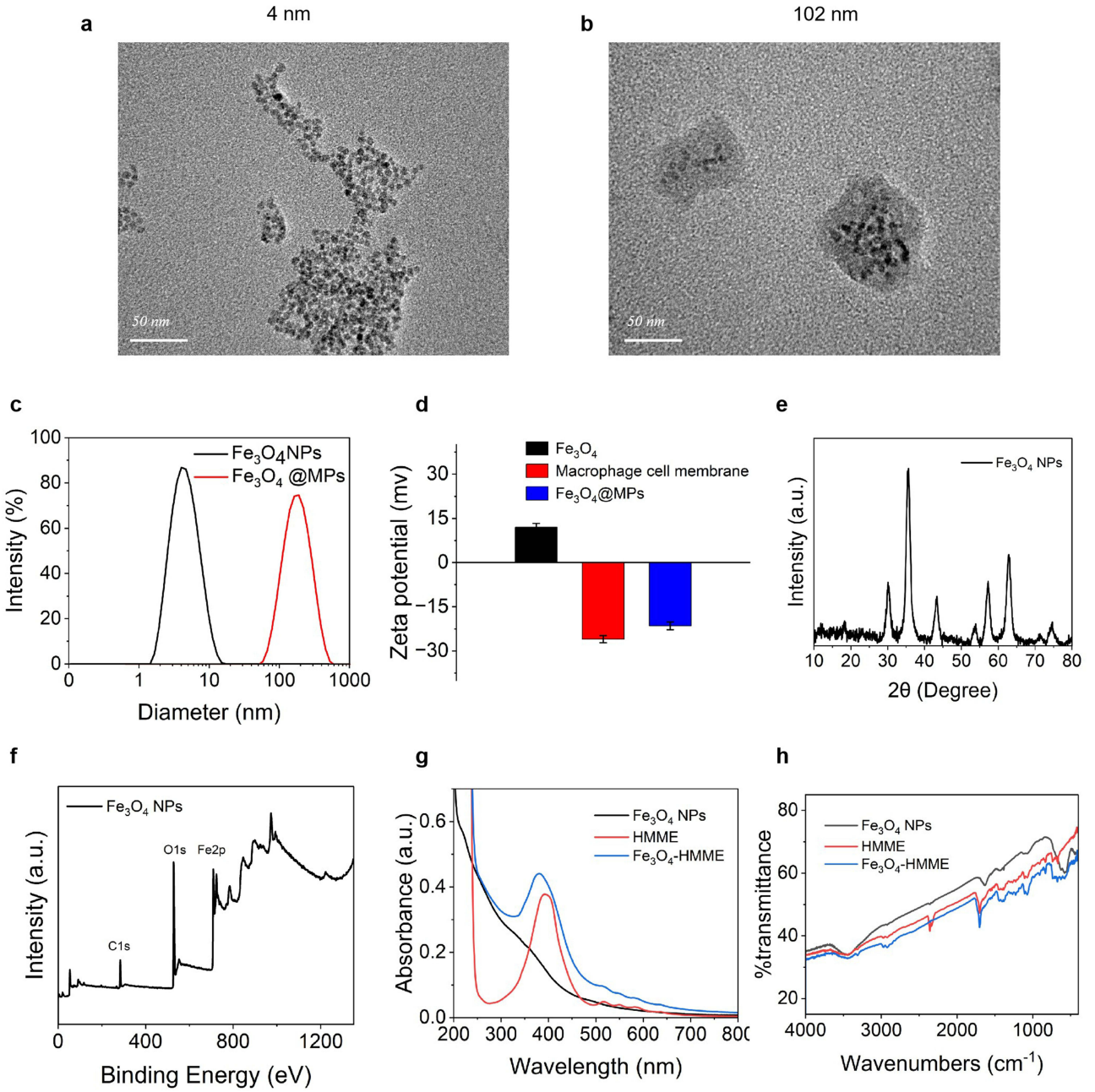

Figure 1 TEM images of (**a**) Fe3O4 NPs and (**b**) Fe3O4@MPs. (**c**) The particle size distribution of Fe3O4 NPs and Fe3O4@MPs. (**d**) The Zeta potential of Fe3O4 NPs, Macrophage cell membrane and Fe3O4@MPs. (**e**) XRD graphs of Fe3O4 NPs. (**f**) XPS graphs of Fe3O4 NPs. (**g**) UV absorption of Fe3O4 NPs, HMME and Fe3O4-HMME. (**h**) Infrared spectra of Fe3O4 NPs, HMME and Fe3O4-HMME.

Cytotoxicity Assessment

To evaluate the in vitro antitumor efficacy of the biomimetic NPs, we first assessed the cytotoxicity of each component against A549 cells using the MTT assay. The results revealed that the cell viability of Fe3O4 group remained above 85% at a concentration as high as 800 μg/mL (Figure 3a). Interestingly, Fe3O4-HMME@MPs without US activation demonstrated lower cytotoxicity compared to the free HMME drug (Figure 3b). As shown in Figure 3c, US treatment alone had negligible effects on cell viability. The Fe3O4-HMME@MPs + US group exhibited the lowest cell viability, a result significantly lower than that of all other control groups. To further investigate the underlying mechanism, we utilized laser scanning confocal microscopy to observe the cellular uptake and subcellular localization of the NPs. As depicted in Figure 3d, after 1 and 4 hours of incubation, the Fe3O4-HMME and Fe3O4-HMME@MPs groups exhibited

https://doi.org/10.2147/IJN.S573349

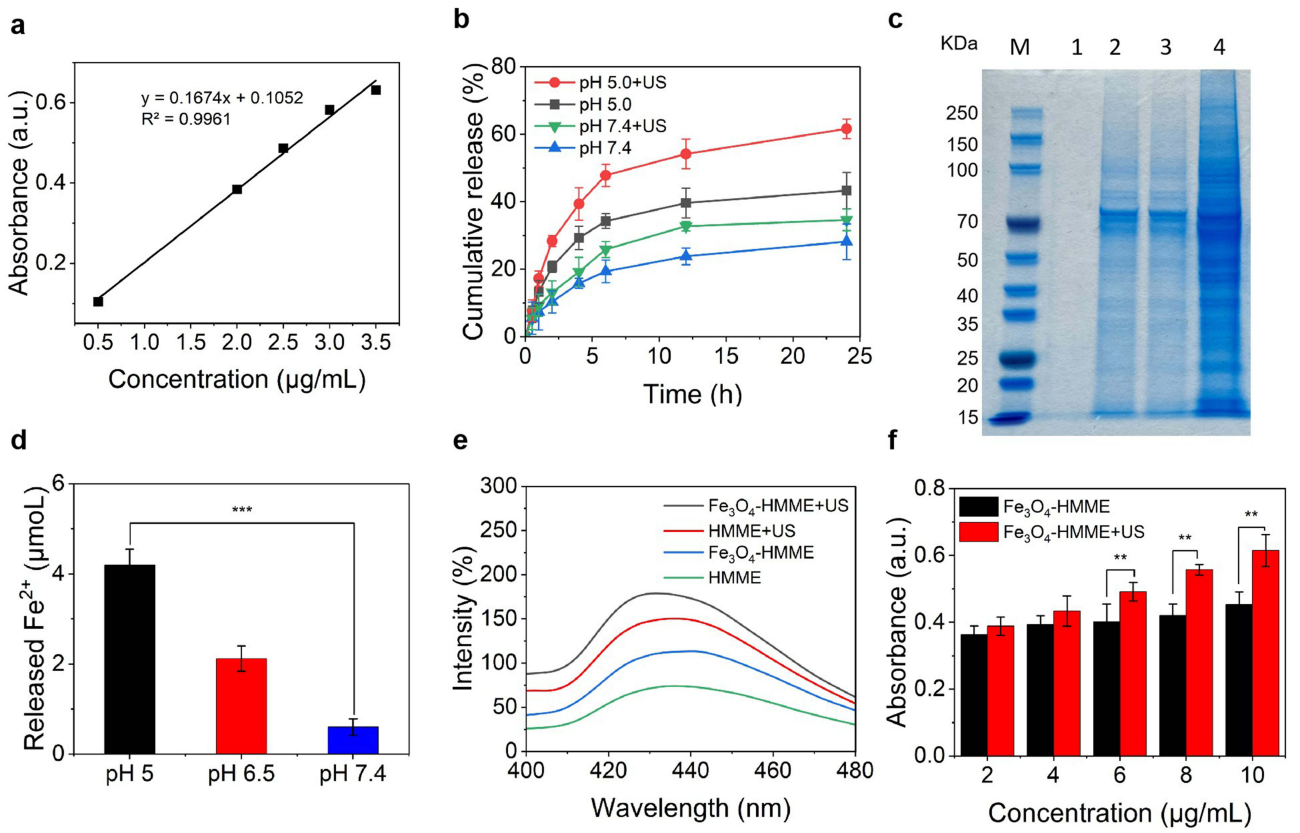

Figure 2 (**a**) HMME standard curve. (**b**) Cumulative release curves of HMME from Fe3O4-HMME in PBS with different pH values (pH 5.0 and 7.4). (**c**) The image of SDS-PAGE: marker, 1Fe3O4 NPs, 2black macrophage cell membrane, 3Fe3O4@MPs, 4Raw264.7 cell. (**d**) Detection of Fe^{2+} released from Fe3O4. (**e**) Detection of •OH produced before and after ultrasound of Fe3O4-HMME. (**f**) Detection of ROS generated by different concentrations of Fe3O4-HMME before and after ultrasound. $^{**}P < 0.01$, $^{***}P < 0.001$.

a gradual increase in intracellular red fluorescence signal compared to free HMME. Notably, a distinct co-localization of the red fluorescence, representing the drug, and the green fluorescence (LysoGreen) labeling lysosomes was observed, manifesting as a yellow signal in the merged images.

Combination of Fe3O4+HMME@MPs with SDT Increased the Levels of ROS and •OH Within A549 Cells

To investigate the mechanism of action of Fe3O4+HMME@MPs, we examined intracellular ROS and •OH generation using confocal microscopy. Figure 4a and b illustrated the intracellular distribution of ROS following different treatments, with green fluorescence representing ROS production. The results indicated that the Free HMME+US, Fe3O4-HMME+US, and Fe3O4-HMME@MPs+US groups exhibited significant green fluorescence signals. The Fe3O4-HMME@MPs+US group displayed the highest fluorescence signal intensity. These signals co-localized with the red fluorescence signal of HMME, and were distinct from Hoechst staining. Figure 4c and d depicted the detection of intracellular •OH. Figure 4c demonstrated that under the same eight treatment conditions, the control, US, and free HMME groups exhibited low red fluorescence intensity (representing •OH). Consistent with the ROS detection results, US treatment enhanced •OH generation. The presence of Fe3O4-HMME and Fe3O4-HMME@MPs further increased the levels of •OH accumulation. The Fe3O4-HMME@MPs+US group exhibited the strongest red fluorescence, suggesting that this combination strategy most effectively generated •OH.

In vivo Distribution of Fe3O4-HMME and Fe3O4-HMME@MPs

To investigate the specific mechanism of the Fe3O4-HMME@MPs combined with SDT treatment regimen, A549 cells were used to establish a lung cancer mouse model. After tumor formation, nude mice were administered the drugs via tail

https://doi.org/10.2147/IJN.S573349

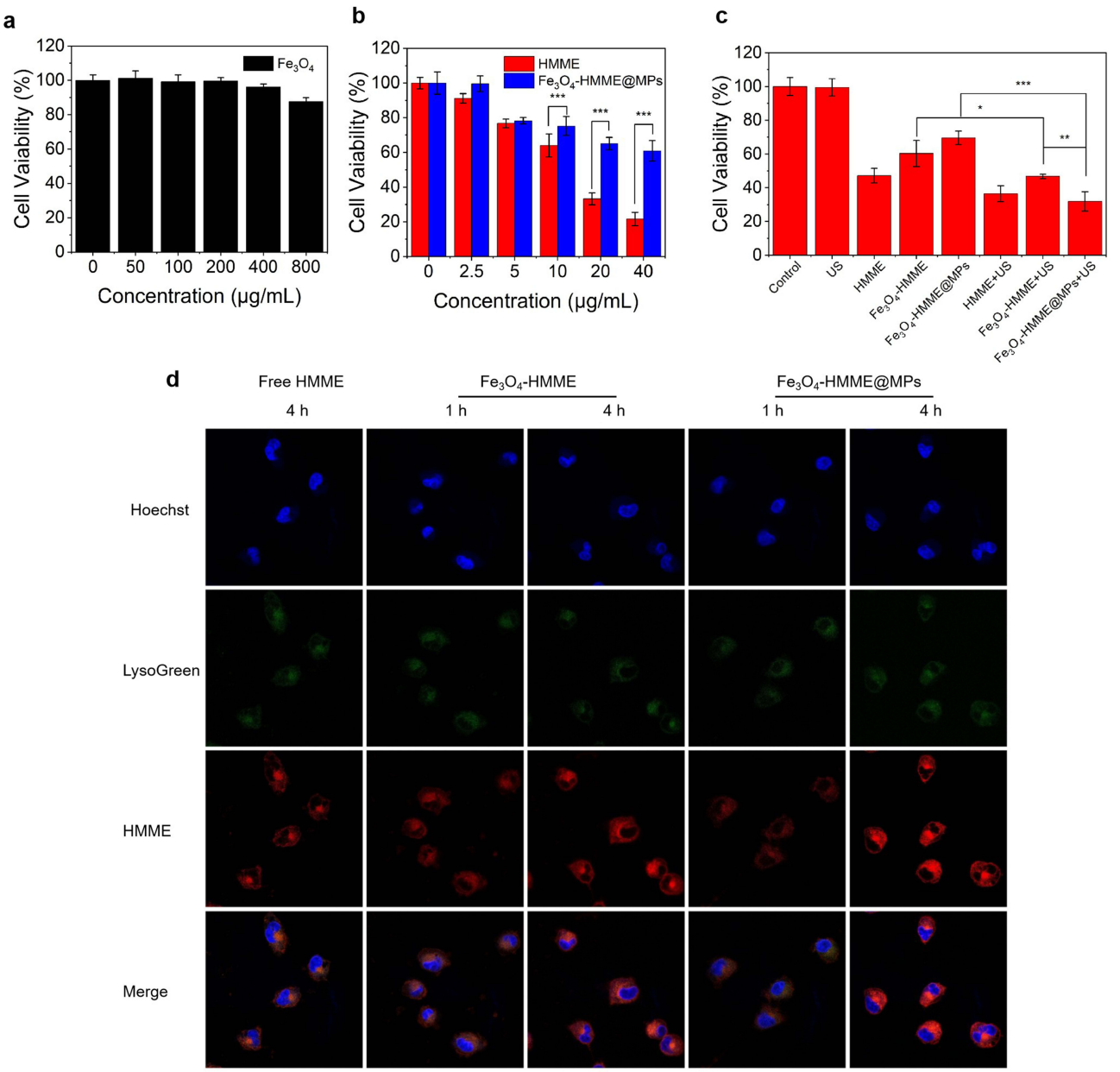

Figure 3 MTT assay for A549 cell viability of (**a**) Fe3O4 NPs, (**b**) free PPIX and Fe3O4-HMME@MPs, (**c**) under different treatments without or with ultrasound (1.75 W/cm2, 5 min). (**d**) Fluorescence images showing the locations of the free HMME, Fe3O4-HMME and Fe3O4-HMME@MPs in A549 cells after incubation for 1 and 4 h: Hoechst (blue), LysoGreen(green), and HMME (red). *$P < 0.05$, **$P < 0.01$, ***$P < 0.001$.

vein injection, followed by US treatment. Fluorescence imaging was performed utilizing the intrinsic fluorescence of HMME. Fe3O4-HMME was used as a control. The results, as shown in Figure 5, indicated that PPIX from the Fe3O4-HMME group primarily accumulated in the liver, lungs, kidneys, and tumor of nude mice. However, the fluorescence in the Fe3O4-HMME@MPs group was mainly concentrated in the tumor. The HMME fluorescence intensity in the major organs of this group was lower than that of the Fe3O4-HMME group within 48 h. We also evaluated the therapeutic effect of SDT and Fe3O4-HMME@MPs by HE staining. The results showed that the Fe3O4-HMME@MPs+US group exhibited the least damage to the major organs (Figure S1).

Therapeutic Effect of Fe3O4-HMME@MPs

To investigate the therapeutic efficacy of the Fe3O4-HMME@MPs combined with SDT treatment strategy, tumor-bearing nude mice models of lung cancer were established. At the end of the treatment, the mice in the Fe3O4-HMME

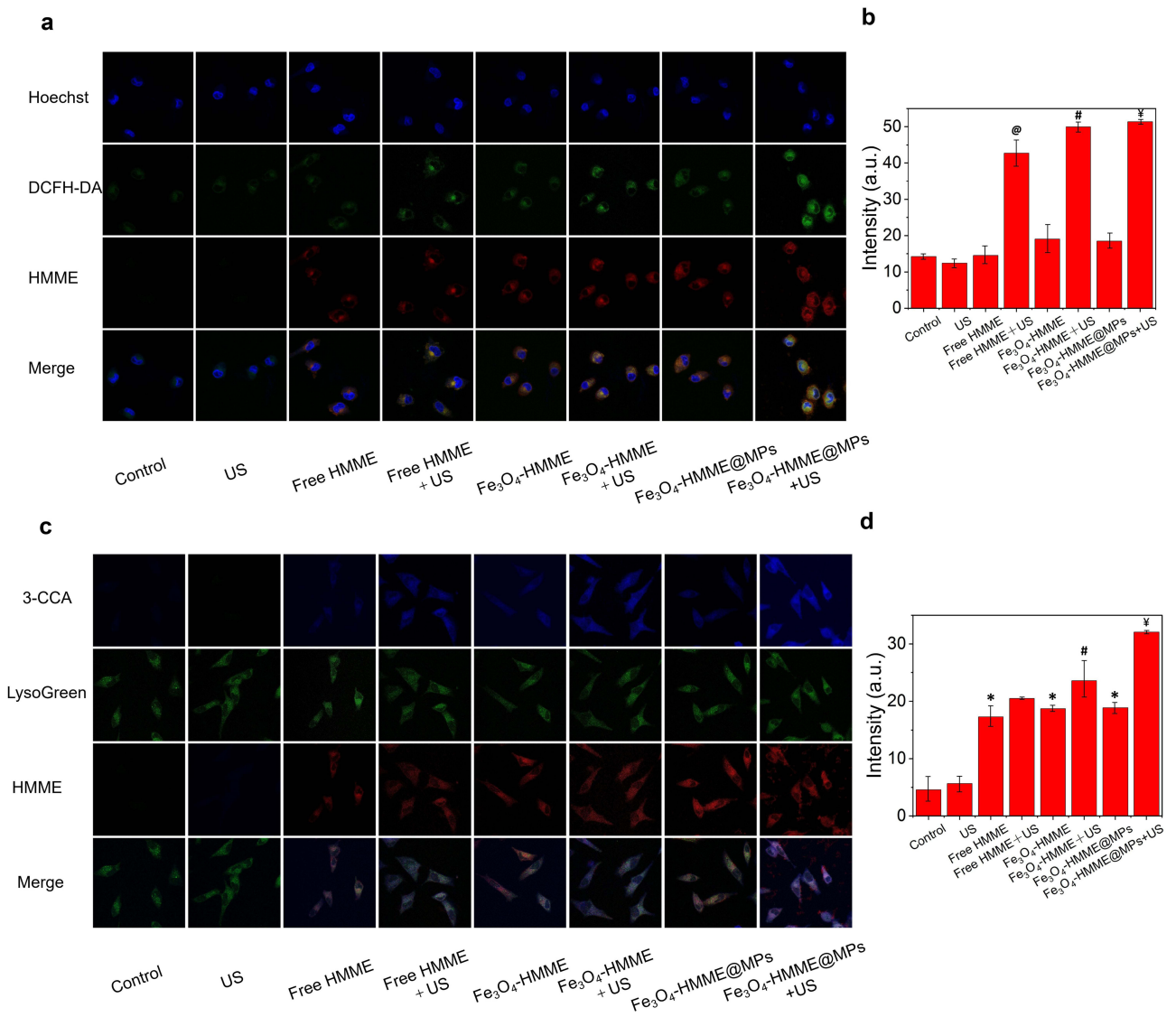

Figure 4 (**a**) Detection of ROS by a confocal microscope. (**b**) Quantified analysis of fluorescence intensity in panel a. (**c**) Detection of intracellular •OH by a confocal microscope. (**d**) Quantified analysis of fluorescence intensity in panel c. Compared with the US group *p<0.05. Compared with the Free HMME group @p<0.05. Compared with the Fe3O4-HMME group #p<0.05. Compared with the Fe3O4-HMME@MPs group ¥p<0.05.

@MPs+US group exhibited the lowest tumor weight (Figure 6b). Notably, during the treatment period, tumor volume was minimized in the Fe3O4-HMME@MPs+US group (Figure 6a and c). Regarding mouse body weight changes, we observed no significant trend in body weight differences among the tumor-bearing nude mice treated with different regimens throughout the culture period (Figure 6d). HE staining further confirmed that the combined treatment strategy of Fe3O4-HMME@MPs and US demonstrated superior therapeutic effects in lung cancer-bearing nude mice (Figure 6e). Furthermore, immunohistochemical analysis revealed the highest prevalence of Perls-DAB and Tunel positive staining, along with the lowest positive levels of Ki67 and GPX4, within the tumors of nude mice in the Fe3O4-HMME@MPs +US group.

Discussions

Lung cancer is the second most common cancer globally and the leading cause of cancer-related mortality. Although existing therapeutic modalities such as surgery, radiotherapy, and chemotherapy have improved patient survival rates to some extent, they are still plagued by issues including limited efficacy and significant side effects.[1,3,6,24] Therefore, the

https://doi.org/10.2147/IJN.S573349

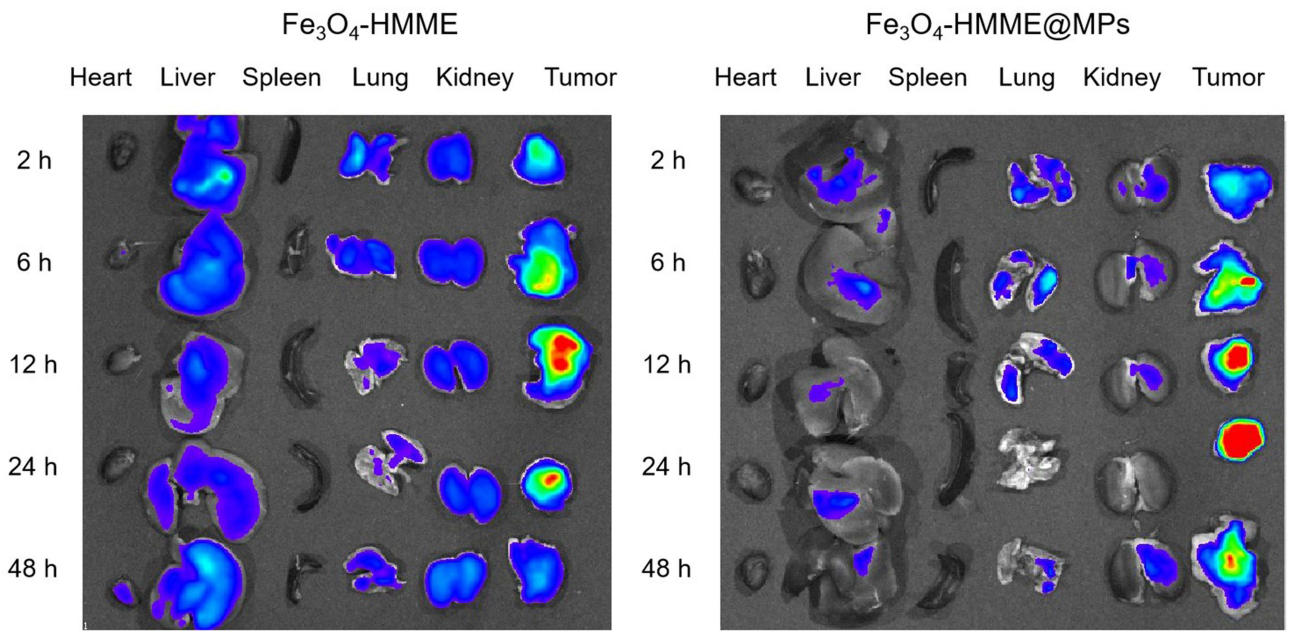

Figure 5 Ex vivo fluorescence images of excised organs and tumors showing the biodistribution of free HMME and Fe3O4-HMME@MPs.

development of novel therapeutic strategies is of paramount importance. In this study, we constructed macrophage membrane-camouflaged Fe3O4-HMME NPs and combined them with SDT. Our research aims to enhance the therapeutic efficacy against lung cancer.

Ferroptosis is a form of regulated cell death characterized by the iron-dependent accumulation of lipid peroxides to lethal levels. Numerous studies have demonstrated that the effective regulation of this cell death modality inhibits the progression of various tumors, such as triple-negative breast cancer, ovarian cancer, and gastrointestinal tumors.[25–27] The study by Yuan et al confirmed that the YTHDC1/FSP1 pathway regulates the ferroptosis process to suppress lung cancer development.[28] Research by Ma et al indicated that targeting CPT1A to induce ferroptosis in tumor cells exerts a synergistic therapeutic effect with immunotherapy for lung cancer.[29] Based on the inhibitory effect of ferroptosis on cancer progression, Fe3O4 is considered an effective therapeutic material. It provides an iron source for ferroptosis. Furthermore, Fe3O4 promotes lipid peroxidation and decreases GPX4 protein levels within ferroptosis-related pathways.[30] Zhang et al constructed Fe3O4 NPs (Fe3O4-PASP-DOX) for triple-negative breast cancer to enhance the efficacy of chemotherapy by augmenting the ferroptotic effect.[31] Building on this foundation and referring to the work of Tian et al, we constructed Fe3O4-HMME@MPs and confirmed their structure through characterization.[32] At the cellular level, we further investigated the synergistic antitumor mechanism of this nanosystem. The MTT assay clearly demonstrated that Fe3O4-HMME@MPs exhibited potent cytotoxicity upon US activation, which indicated the successful initiation of SDT. Confocal laser scanning microscopy revealed that the NPs were efficiently endocytosed by cells and accumulated in lysosomes. This location is not only a key site for drug release but also creates ideal conditions for the reduction of Fe^{3+} to Fe^{2+}, thereby initiating the Fenton reaction. Crucially, fluorescence detection of intracellular ROS and •OH visually confirmed that the combined treatment of Fe3O4-HMME@MPs and US generated high levels of reactive oxygen species. In vivo evidence—including increased Perls-DAB positive staining indicating iron accumulation, an elevation in TUNEL-positive signals suggesting enhanced apoptosis, and decreased Ki67 and GPX4 expression indicating a greater tumor-suppressive effect—collectively explained the superior therapeutic performance of the Fe3O4-HMME@MPs+US group. This mechanism is consistent with the synergistic action models of Fe3O4 NPs combined with drugs, as reported by Yu et al and Yang et al. This also strongly suggests a significant synergistic effect between the Fe3O4 core-mediated ferroptosis and the HMME-mediated SDT.[33,34] Based on these findings, we posit that the combination of Fe3O4-HMME@MPs and SDT collectively demonstrates a potent tumor cell-killing capacity. This approach effectively overcomes the limitations of monotherapies for lung cancer, particularly under hypoxic conditions.

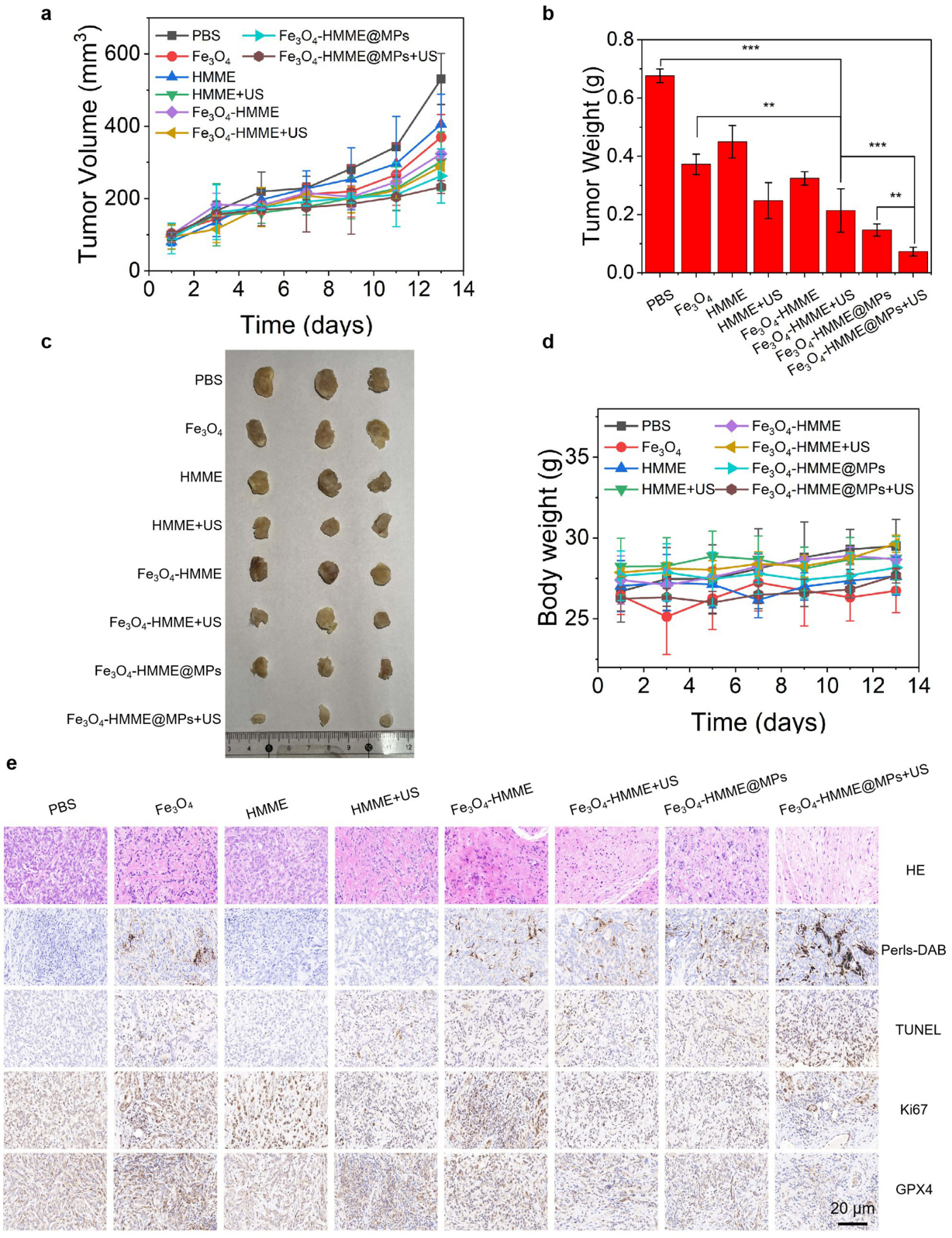

Figure 6 (**a**) Changes of tumor volume of all nude mice during treatment. (**b**) The average tumor weights of each group at the end of treatment. (**c**) Digital images of the tumors at the end of treatment. (**d**) Changes of body weights of all nude mice during treatment. (**e**) H&E staining, Perls-DAB staining, TUNEL staining, ki67 staining and GPX4 immunohistochemical staining of tumor tissues after different treatments, Scale bar = 20 μm, n=3.

https://doi.org/10.2147/IJN.S573349

Compared to existing studies, our system demonstrates significant advantages. Traditional SDT is often hindered by tumor hypoxia, which suppresses the generation of ROS. To address this issue, research focusing on the use of photosensitizers has been on the rise. For instance, the HMME/R837@Lip system developed by Yue et al has been shown to effectively inhibit the growth of primary tumors while also preventing the occurrence of lung metastases.[35] Additionally, research by Du et al indicated a synergistic effect when HMME was combined with Fe3O4 in a nanodelivery system under near-infrared laser irradiation.[36] Inspired by these findings, we applied a macrophage membrane biomimetic strategy in conjunction with the photosensitizer to inhibit lung cancer. In vivo distribution experiments clearly demonstrated its decisive advantages: compared to free NPs, Fe3O4-HMME@MPs significantly reduced nonspecific accumulation in reticuloendothelial system organs such as the liver and lungs, while markedly enhancing targeted enrichment at the tumor site. This result aligns closely with the research trends observed by Wang et al and Zhao et al regarding cell membrane biomimetic nanomedicines.[37,38] Our study not only directly explains the superior therapeutic effects observed in animal models but also suggests lower systemic toxicity, providing a reliable delivery mechanism for achieving precise and efficient tumor treatment.

Ultimately, the in vivo antitumor experiments provide robust support for the clinical application prospects of this synergistic therapeutic strategy. In the tumor-bearing mouse model, the Fe3O4-HMME@MPs+US treatment group exhibited the strongest tumor suppression effects, with the lowest tumor volume and weight among all groups. In-depth histopathological and immunohistochemical analyses further elucidated the underlying mechanisms: HE staining confirmed extensive tumor necrosis, while Perls-DAB staining, TUNEL analysis, and changes in Ki67 and GPX4 protein expression collectively validated the effective activation of ferroptosis and apoptosis, as well as significant inhibition of

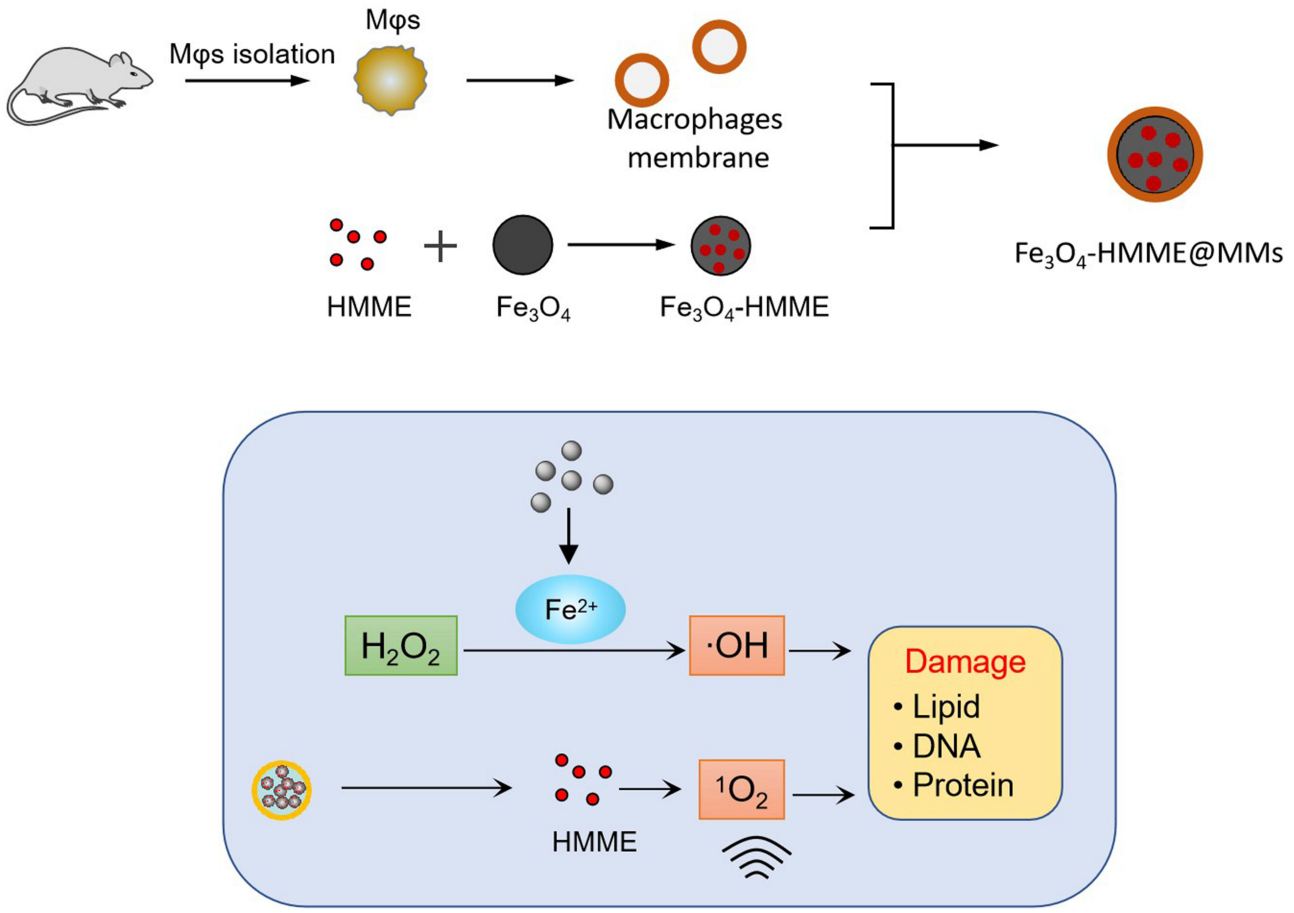

Figure 7 Schematic illustration of the fabrication of Fe3O4-HMME@MMs biomimetic nanoplatform and its mechanism of action for synergistic ferroptosis and sonodynamic therapy in lung cancer cells.

tumor proliferation. Moreover, the magnetic properties of Fe3O4 present potential opportunities for integrated imaging and therapy, which could facilitate the development of theranostics. To achieve clinical translation, long-term, multi-species toxicological assessments, dose-response studies, and reproducibility research are necessary, along with broader animal model validations targeting different lung cancer subtypes. Additionally, it is essential to explore the optimization of membrane coating density, loading capacity, and drug release kinetics, as well as the potential for combination with other therapeutic modalities such as radiotherapy, chemotherapy, and immunotherapy.

Conclusion

In summary, this study successfully constructed a biomimetic nanoplatform, Fe_3O_4-HMME@MPs, with excellent targeting capabilities and synergistic therapeutic efficacy. This offers a novel strategy and approach for the precision therapy of lung cancer. This research not only validates the efficacy of combining ferroptosis with SDT for the treatment of lung cancer but also serves as a valuable reference for the future development and application of nanomedicines (Figure 7). We believe that with the continuous advancement of nanotechnology, nanomedicines will play an increasingly important role in the field of cancer therapy.

Ethics Statement

The animal study complied with ethical regulations and was approved by the Experimental Animal Ethics Committee of Jiangsu University (IACUC Number: KY-20230127). All experiments complied with the Chinese Law on Laboratory Animal Welfare (Guideline for Ethical Review of Animal Welfare, Standard number: GB/T 35892-2018).

Acknowledgments

We are deeply grateful to Jiangsu University Laboratory Animal Research Center for their essential contribution to this research, particularly for providing the animal experimental facilities and conducting key testing procedures. We extend our sincere thanks to Prof. Cui Junming for their expert guidance and technical assistance during the in vivo studies. The ethical approval for this work was obtained from Jiangsu University's Institutional Animal Care and Use Committee (IACUC Number: KY-20230127).

Disclosure

The authors report no conflicts of interest in this work.

References

1. Smolarz B, Łukasiewicz H, Samulak D, et al. Lung cancer—epidemiology, pathogenesis, treatment and molecular aspect (Review of Literature. *Int J Mol Sci*. 2025;26(5):2049. doi:10.3390/ijms26052049
2. Jeon H, Wang S, Song J, et al. Update 2025: management of non-small-cell lung cancer. *Lung*. 2025;203(1):53. doi:10.1007/s00408-025-00801-x
3. Bouchard N, Daaboul N. Lung cancer: targeted therapy in 2025. *Current Oncol*. 2025;32(3):146. doi:10.3390/curroncol32030146
4. Tian Y, Ma R, Zhao W, et al. Comprehensive characterization of early-onset lung cancer, in Chinese young adults. *Nat Commun*. 2025;16(1):1976. doi:10.1038/s41467-025-57309-4
5. Wang C, Chen B, Liang S, et al. China Protocol for early screening, precise diagnosis, and individualized treatment of lung cancer. *Signal Transduct Target Therap*. 2025;10(1):175. doi:10.1038/s41392-025-02256-1
6. Abu Rous F, K SE, Sridhar A, et al. Lung cancer treatment advances in 2022. *Cancer Invest*. 2023;41(1):12–24. doi:10.1080/07357907.2022.2119479
7. Li Y, Yan B, He S. Advances and challenges in the treatment of lung cancer. *Biomed Pharmacother*. 2023;169:115891. doi:10.1016/j.biopha.2023.115891
8. Florez N, Kiel L, Riano I, et al. Lung cancer in women: the past, present, and future. *Clin Lung Cancer*. 2024;25(1):1–8. doi:10.1016/j.cllc.2023.10.007
9. Piro NS, Hamad SM, Mohammed AS, et al. Green synthesis magnetite (Fe_3O_4) nanoparticles from *Rhus coriaria* extract: a characteristic comparison with a conventional chemical method. *IEEE Trans Nanobiosci*. 2023;22(2):308–317. doi:10.1109/TNB.2022.3187344
10. Qi X, Yao M, Jin M, et al. Application of magnetic resonance imaging based on Fe 3 O 4 nanoparticles in the treatment of cerebrovascular diseases. *J Nanosci Nanotechnol*. 2021;21(2):843–851. doi:10.1166/jnn.2021.18697
11. Huang C, Chang E, Zheng L, et al. Tumor protease-activated theranostic nanoparticles for MRI-guided glioblastoma therapy. *Theranostics*. 2023;13(6):1745–1758. doi:10.7150/thno.79342
12. Song N, Zhang J, Zhai J, et al. Ferritin: a multifunctional nanoplatform for biological detection, imaging diagnosis, and drug delivery. *Acc Chem Res*. 2021;54(17):3313–3325. doi:10.1021/acs.accounts.1c00267

13. Mikhailidi A, Ungureanu E, Belosinschi D, et al. Cellulose-based metallogels—part 3: multifunctional materials. *Gels*. 2023;9(11):878. doi:10.3390/gels9110878
14. Wang Y, Wu X, Bao X, et al. Progress in the mechanism of the effect of Fe3O4 nanomaterials on ferroptosis in tumor cells. *Molecules*. 2023;28(11):4562. doi:10.3390/molecules28114562
15. P SS, Samal S, Sahu R, et al. Advances in nanotechnology for colorectal cancer: a smart targeting and theranostics approach. *Med Oncol*. 2025;42(8):346. doi:10.1007/s12032-025-02910-2
16. Nejadnik H, Tseng J, Daldrup Link H. Magnetic resonance imaging of stem cell–macrophage interactions with ferumoxytol and ferumoxytol-derived nanoparticles. Wiley interdisciplinary reviews. *Nanomed Nanobiotechnol*. 2019;11(4):e1552. doi:10.1002/wnan.1552
17. Xu M, Zhou L, Zheng L, et al. Sonodynamic therapy-derived multimodal synergistic cancer therapy. *Cancer Lett*. 2021;497:229–242. doi:10.1016/j.canlet.2020.10.037
18. Guo J, Pan X, Wang C, et al. Molecular imaging-guided sonodynamic therapy. *Bioconjugate Chem*. 2022;33(6):993–1010. doi:10.1021/acs.bioconjchem.1c00288
19. Cao J, Sun Y, Zhang C, et al. Tablet-like TiO(2)/C nanocomposites for repeated type I sonodynamic therapy of pancreatic cancer. *Acta Biomater*. 2021;129:269–279. doi:10.1016/j.actbio.2021.05.029
20. Gong J, Cheng D, Liu C, et al. Hybrid cell membrane-coated nanoparticles for synergizing sonodynamic therapy and immunotherapy against triple-negative breast cancer. *Adv Healthcare Mater*. 2025;14(3):e2404184. doi:10.1002/adhm.202404184
21. Xu J, Pei Z, Wang Y, et al. Bioactive microspheres to enhance sonodynamic-embolization-metalloimmune therapy for orthotopic liver cancer. *Biomaterials*. 2025;317:123063. doi:10.1016/j.biomaterials.2024.123063
22. Diao P, Han C, Li X, et al. Hematoporphyrin monomethyl ether photodynamic therapy of port wine stain. *Narrative Review*. 2023;16:1135–1144.
23. Lazarov T, Juarez-Carreño S, Cox N, et al. Physiology and diseases of tissue-resident macrophages. *Nature*. 2023;618(7966):698–707. doi:10.1038/s41586-023-06002-x
24. Li Y, Wu X, Yang P, et al. Machine learning for lung cancer diagnosis, treatment, and prognosis. *Genomics Proteomics Bioinformatics*. 2022;20(5):850–866. doi:10.1016/j.gpb.2022.11.003
25. Yang F, Xiao Y, Ding J, et al. Abstract P6-11-13: ferroptosis heterogeneity in triple-negative breast cancer reveals an innovative immunotherapy combination strategy. *Cancer Res*. 2023;83(5_Supplement):P6.
26. Guo K, Lu M, Bi J, et al. Ferroptosis: mechanism, immunotherapy and role in ovarian cancer. *Front Immunol*. 2024;15:1410018. doi:10.3389/fimmu.2024.1410018
27. Zhang R, Kang R, Tang D. Ferroptosis in gastrointestinal cancer: from mechanisms to implications. *Cancer Lett*. 2023;561:216147. doi:10.1016/j.canlet.2023.216147
28. Yuan S, Xi S, Weng H, et al. YTHDC1 as a tumor progression suppressor through modulating FSP1-dependent ferroptosis suppression in lung cancer. *Cell Death Differ*. 2023;30(12):2477–2490. doi:10.1038/s41418-023-01234-w
29. Ma L, Chen C, Zhao C, et al. Targeting carnitine palmitoyl transferase 1A (CPT1A) induces ferroptosis and synergizes with immunotherapy in lung cancer. *Signal Transduct Target Therap*. 2024;9(1):15–64. doi:10.1038/s41392-024-01772-w
30. Zhang Z, Zhao Y, Wang Y, et al. Autophagy/ferroptosis in colorectal cancer: carcinogenic view and nanoparticle-mediated cell death regulation. *Environ Res*. 2023;238(Pt 2):117006. doi:10.1016/j.envres.2023.117006
31. Zhang J, Zhou K, Lin J, et al. Ferroptosis-enhanced chemotherapy for triple-negative breast cancer with magnetic composite nanoparticles. *Biomaterials*. 2023;303:122395. doi:10.1016/j.biomaterials.2023.122395
32. Tian X, Ruan L, Zhou S, et al. Appropriate size of Fe_3O_4 nanoparticles for cancer therapy by ferroptosis. *ACS Appl Bio Mater*. 2022;5(4):1692–1699. doi:10.1021/acsabm.2c00068
33. Yu K, Chen Y, Zhang L, et al. Cancer-erythrocyte membrane-mimicking Fe 3 O 4 nanoparticles and DHJS for ferroptosis/immunotherapy synergism in tumors. *ACS Appl Mater Interfaces*. 2023;15(38):44689–44710. doi:10.1021/acsami.3c07379
34. Yang H, Li G, Zhang J, et al. A novel hollow iron nanoparticle system loading PEG-Fe(3)O(4) with C5a receptor antagonist for breast cancer treatment. *Front Immunol*. 2024;15:1466180. doi:10.3389/fimmu.2024.1466180
35. Yue W, Chen L, Yu L, et al. Checkpoint blockade and nanosonosensitizer-augmented noninvasive sonodynamic therapy combination reduces tumour growth and metastases in mice. *Nat Commun*. 2019;10(1):2015–2025. doi:10.1038/s41467-019-09760-3
36. Du S, Zhang L, Han K, et al. Combined phycocyanin and hematoporphyrin monomethyl ether for breast cancer treatment via photosensitizers modified Fe_3O_4 nanoparticles inhibiting the proliferation and migration of MCF-7 cells. *Biomacromolecules*. 2018;19(1):31–41. doi:10.1021/acs.biomac.7b01197
37. Wang J, Liang S, Chen S, et al. Bacterial outer membrane vesicle-cancer cell hybrid membrane-coated nanoparticles for sonodynamic therapy in the treatment of breast cancer bone metastasis. *J Nanobiotechnol*. 2024;22(1):328. doi:10.1186/s12951-024-02619-w
38. Zhao J, Yu B, Li L, et al. Outer membrane vesicle–cancer hybrid membrane coating indocyanine green nanoparticles for enhancing photothermal therapy efficacy in tumors. *ACS Biomater Sci Eng*. 2024;10(12):7619–7631. doi:10.1021/acsbiomaterials.4c01251